

HEMODYNAMICS OF CORONARY ARTERY ANEURYSMS IN KAWASAKI DISEASE —
AN IDEALIZED ANEURYSM MODEL

An Honors Thesis Submitted to
Biomedical Computation
in partial fulfillment of the Honors Program
STANFORD UNIVERSITY

by

ALEXANDER LU
May 24, 2019

HEMODYNAMICS OF CORONARY ARTERY ANEURYSMS IN KAWASAKI DISEASE —
AN IDEALIZED ANEURYSM MODEL

by

Alexander Lu

May 24, 2019

Approved:

Alison Marsden, Ph.D

Date

Research Advisor from the Department of Bioengineering

Approved:

James Priest, MD.

Date

Faculty Reader from the Department of Pediatrics (Cardiology)

Approved:

Russ Altman, Ph.D., MD. (Do not need to obtain signature)

Date

Faculty Chair of Program in Biomedical Computation

Contents

1	ABSTRACT.....	1
2	INTRODUCTION	2
3	METHODOLOGY	3
3.1	IDEALIZED ANEURYSM MODELS	3
3.2	COMPUTATIONAL HEMODYNAMICS	4
3.3	RESIDENCE TIME CALCULATION.....	5
3.4	POST-SIMULATION ANALYSIS.....	5
4	RESULTS	7
4.1	HEMODYNAMIC VARIATIONS WITH SHAPE AND DIAMETER	7
4.2	ANEURYSM POSITION AND HEMODYNAMICS	9
5	DISCUSSION	13
6	ACKNOWLEDGEMENTS.....	15
7	REFERENCES.....	16

1 Abstract

Kawasaki Disease (KD), a vasculitis of unknown etiology typically occurring in infants and young children, is the leading cause of acquired heart disease in childhood in developed countries. Approximately 20-25% of patients may eventually develop coronary artery aneurysms (CAAs) if not treated within ten days of onset [1-6]. Abnormal hemodynamics within CAAs may trigger thrombosis, resulting in myocardial infarction and sudden death [3-8]. Although prior studies have investigated the use of hemodynamic parameters derived from patient-specific computational hemodynamic simulations for stratifying patient thrombotic risk, such studies have been limited in cohort size. Here, we present a pipeline for systematic analysis of how aneurysm geometry (i.e. aneurysm diameter, length, and position) affects hemodynamics. The pipeline supports the generation of artificial aneurysms from a baseline patient coronary tree, interfacing with the Simvascular open-source software. The pipeline also provides post-processing and data analysis capabilities. Through this systematic analysis, we elucidate the complementary roles of aneurysm diameter, length, and position on hemodynamic parameters such as time-averaged wall shear stress and residence time. We find that multiple combinations of diameter and length can illicit similar flow behavior. Further, we propose that vessel curvature underlies the effects of aneurysm position. Overall, we demonstrate the promise of systematic investigation of the relationship between aneurysm geometry and flow behavior, a general proof-of-concept for systematically evaluating pathological hemodynamics in the absence of clinical data and assessing hemodynamic parameter sensitivity with respect to patient anatomy.

2 Introduction

Kawasaki Disease (KD), a vasculitis of unknown etiology typically occurring in infants and young children, is the leading cause of acquired heart disease in childhood in developed countries. Approximately 20-25% of patients may eventually develop coronary artery aneurysms (CAAs) if not treated within ten days of disease onset [1-6]. Unlike cerebral or abdominal aorta aneurysms, which pose a risk of rupture, CAAs are threatening in their potential for inducing thrombus formation, resulting in myocardial infarction and sudden death [3-8].

CAAs resulting from KD can adopt a wide range of shapes and diameters across a range of locations within the coronary tree [1, 2, 4]. Size classification often relies on maximum aneurysm diameter, with potential normalization based on body surface area (Z-score) to label aneurysms as uninvolved, small, medium, or giant. CAAs may also be roughly classified by shape into groups such as saccular, fusiform, and string-of-pearls. A final classification is based on the number of major coronary vessels which bear aneurysms [1, 2]. Coupled with interpatient variability in hemodynamic factors such as blood pressure and cardiac output, wide variability in aneurysm diameter, shape, and position amplifies difficulty in isolating the effects of geometric parameters. Indeed, complex geometry, as well as aneurysm shape, number, and location, may all contribute to abnormal hemodynamics and correlate with patient outcome.

Presently, the American Heart Association offers guidelines for stratification of patient thrombotic risk that rely on aneurysm diameter alone as the criterion for initiating systemic anticoagulation; however studies suggest risk may also depend on hemodynamic parameters such as time-averaged wall shear stress (TAWSS), residence time (RT), and oscillatory shear index (OSI), which are not available through image data alone [9-13]. Patient-specific hemodynamic simulations can non-invasively supply informative hemodynamic parameters for better thrombotic risk assessment; however, existing studies have been limited in patient cohort size and struggle to quantify effects of aneurysm shape on local hemodynamics [10-13].

With such limitations in mind, existing patient-specific models can be augmented by introducing artificial aneurysms of specified length and diameter, to achieve a systematic evaluation of relationship between CAA shape, diameter, and position on local hemodynamics. Ultimately, elucidating the relationship between hemodynamics and aneurysmal shape characteristics may underlie more powerful risk stratification methods to support clinical decision-making regarding initiation of anticoagulation therapy.

3 Methodology

3.1 Idealized Aneurysm Models

A pipeline for generation of three-dimensional idealized aneurysm models has been constructed with dependencies on the Visualization ToolKit Package (VTK). The pipeline workflow consists of the following three steps.

(1) **Baseline Model** An existing patient-specific model of the aorta and coronary vasculature was constructed from coronary CT image data in Simvascular, an open source software which provides a full pipeline for patient-specific cardiovascular simulation [14]. This baseline model is constructed through manual identification of preliminary vessel centerlines, 2D segmentation of vessel contours, and lofting contours to form vessel walls. The union of all vessel walls is taken as the three-dimensional model, represented as a triangular mesh in 3D space.

(2) **Surface Parameterization** Vessel centerlines are re-extracted from the three-dimensional model in Simvascular, then upsampled from cubic spline interpolation to achieve sufficient spatial resolution in the centerline's discretization. Points from the 3D model's wall are expressed in terms of distance along the centerline, $s(t)$, by mapping each wall point to the resampled centerline point that minimizes L_2 distance. The Frenet-Serret reference frame is then constructed from the centerline to label each wall point with its angle $\phi(t) \in [-\pi, \pi]$ with respect to the centerline's unit normal $\mathbf{n}(t)$. This combination of position and angle with respect to the centerline enables efficient generation of artificial aneurysms.

(3) **Aneurysm Generation** Existing AHA aneurysm classification for small, medium, and giant CAAAs serves as a guide to proceed from body surface area-normalized Z-score to an estimated maximal diameter for a given coronary vessel. The Z-score formulation presented in Dallaire and Dahdah et al. 2011 [15],

$$Z = \frac{CA_{obs} - [a + (b \times \sqrt{BSA})]}{a_{SE} + (b_{SE} \times \sqrt{BSA})}$$

with coefficients a, b, a_{SE}, b_{SE} estimated separately for each vessel. Using aneurysmal shape index (ASI), defined as the ratio of aneurysmal length to maximal lumen diameter,

$$ASI = \frac{\text{aneurysm length}}{\text{aneurysm diameter}}$$

we obtain a range of lengths and diameters to guide aneurysm generation [13].

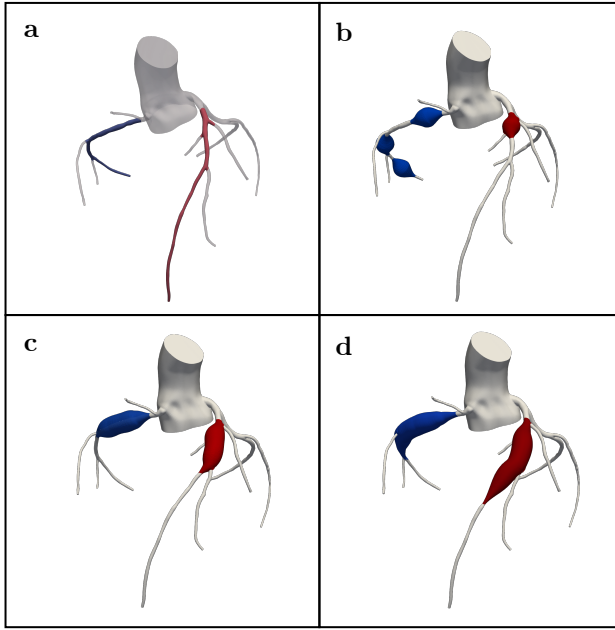


Figure 1: A baseline model serves as the basis for producing idealized aneurysms with varying positions, lengths, diameters. **a.** Baseline model of aorta, coronary vasculature with RCA, LAD highlighted. **b.** Aneurysms with shape index of 2 generated at 3 positions along the RCA, and at 1 position in the LAD. **c.** **d.** Aneurysms with shape index 4, 6 respectively generated at 1 position each along RCA, LAD.

For a given target length and maximum diameter, we can use the position and angle parameterizations determined in step (2) to deform the vessel wall. Deformation magnitude is given through second-order smooth interpolation of diameter as a function of centerline position, producing radial symmetry. In the case of vessel branching from the desired aneurysm region, all points of the bifurcating vessel and its branches are shifted and rotated according to the average deformation at the bifurcation. Empirically, this method has worked best to control bifurcation angle between baseline and artificial aneurysms of varying shape and maximal diameter. This process was applied for multiple positions, shapes, and diameters, as exemplified in **Figure 1**.

3.2 Computational Hemodynamics

Generated aneurysm models are further processed in Simvascular using Tetgen, an open source package for mesh generation included in Simvascular [16]. Tetrahedral finite element meshes with boundary layer meshing are generated for each model. The Simvascular solver then computes a numerical solution to the time-dependent Navier-Stokes equations governing blood flow. Blood is modeled as an incompressible Newtonian fluid (density=1.06 g/cc, dynamic viscosity=0.04 dynes/cm²) and walls are assumed to be rigid in all cases.

Simulation Boundary Conditions Systolic myocardial contraction increases intra-myocardial pressure, transiently increasing distal coronary resistance substantially and causing coronary flow to be out of phase with systemic flow. Specialized boundary conditions coupling intra-myocardial pressure to coronary flow are required to replicate this complex physiology in the numerical model. We achieve this by modeling the heart and distal vasculature with a closed-loop, Lumped Parameter Network (LPN), which imposes boundary conditions with tunable parameters to produce physiologically accurate cardiac output, heart rate, blood pressure, and flow distributions. For all idealized models described in this work, LPN parameters are fixed to better isolate the effects of aneurysmal geometry on hemodynamics. **Figures 1, 2** show the pipeline, proceeding from baseline model to artificial aneurysms and simulation results over isolated aneurysm regions.

3.3 Residence Time Calculation

Although pathways underlying platelet activation and thrombosis remain poorly understood, flow recirculation and stagnation have been hypothesized to contribute to thrombosis [17, 18]. To better understand aneurysm hemodynamics, we can employ Residence Time (RT), which has been shown to be an effective measure of quantifying recirculating flow that traps fluid for an extended duration. RT is computed as described in Esmaily-Moghadam et al. 2013, by first solving the advection-diffusion equation [17]:

$$\frac{\partial \tau}{\partial t} + \mathbf{u} \cdot \nabla \tau - \nabla \cdot \kappa \nabla \tau - H = 0$$

where τ is a measure of time, \mathbf{u} is the velocity field from solving the Navier-Stokes equation; κ is the diffusivity, which is set to 0; H is the particle source term defined as 1 inside the region of interest, Ω_τ , and 0 otherwise. RT is then computed as:

$$RT = \frac{1}{T} \int_{(n-1)T}^{nT} \frac{1}{V_{\Omega_\tau}} \int_{\Omega_\tau} \tau(\mathbf{x}, t) d\Omega dt$$

$$V_{\Omega_\tau} = \int_{\Omega_\tau} d\Omega$$

3.4 Post-Simulation Analysis

In order to quantify local aneurysm hemodynamics we isolate the aneurysm from the larger coronary tree. Aggregate measures of certain hemodynamic quantities, such as WSS, can then be computed either over the aneurysm surface, or over the aneurysm volume. Quantities of interest can also be computed using spatial average over the domain and temporal average over the cardiac cycle. The post-simulation analysis pipeline — including thresholding operations, variable integration, and simulation

data visualization — was developed using custom scripts interfacing with Paraview (<https://www.paraview.org/>), an open-source data-analysis and visualization application.

4 Results

Idealized aneurysms of 3 representative shape index values ($ASI = 2, 4, 6$) were generated for 5 diameters ($z\text{-score} = 6, 8, 10, 12, 14$) at three positions along the right coronary artery (RCA) and one position in the left anterior descending (LAD) for a total of 40 cases. Hemodynamic simulation results were isolated over aneurysmal regions to identify the effects of shape, diameter, and position on local hemodynamic conditions.

4.1 Hemodynamic Variations with Shape and Diameter

Hemodynamic parameter distributions at the vessel wall have been hypothesized to be an effective way to assess aneurysm hemodynamics. Broadly, we expect similarly shaped aneurysms to give rise to similar hemodynamic behaviors; further, we expect that increases in Z -score correspond to decreases in fluid velocity and the potential for turbulence or recirculation. Indeed, these expectations are reflected qualitatively in distributions of TAWSS over the vessel surface (**Figure 2**). We observe that surface

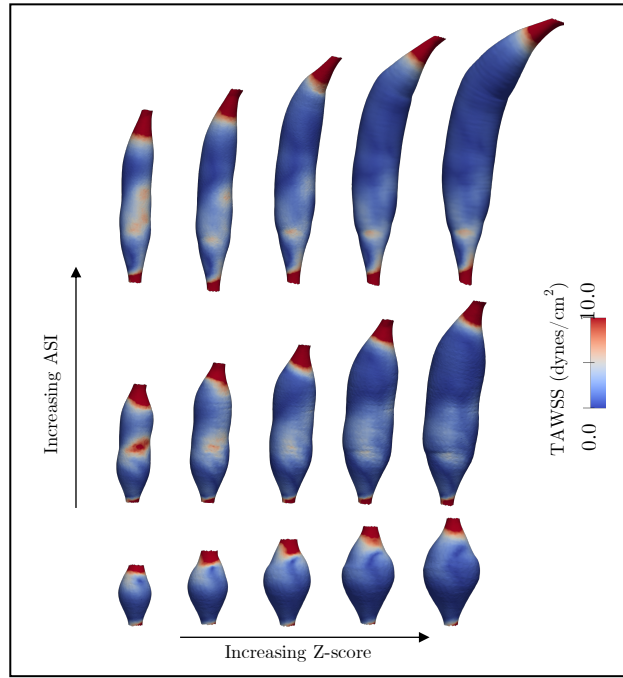


Figure 2: A representative collection of artificial aneurysms generated at 3 ASI values (2, 4, 6) with 5 Z-scores (6, 8, 10, 12, 14) while fixing the aneurysm inlet position at the proximal RCA. The Time-Averaged Wall Shear Stress is displayed over the surface, demonstrating consistent variation of hemodynamic behavior with respect to Z-score.

hemodynamic patterns vary consistently with respect to increasing Z-score, with overall decrease in TAWSS as the diameter increases. Additionally, for each value of ASI, aneurysms appear to bear similar spatial distributions of TAWSS.

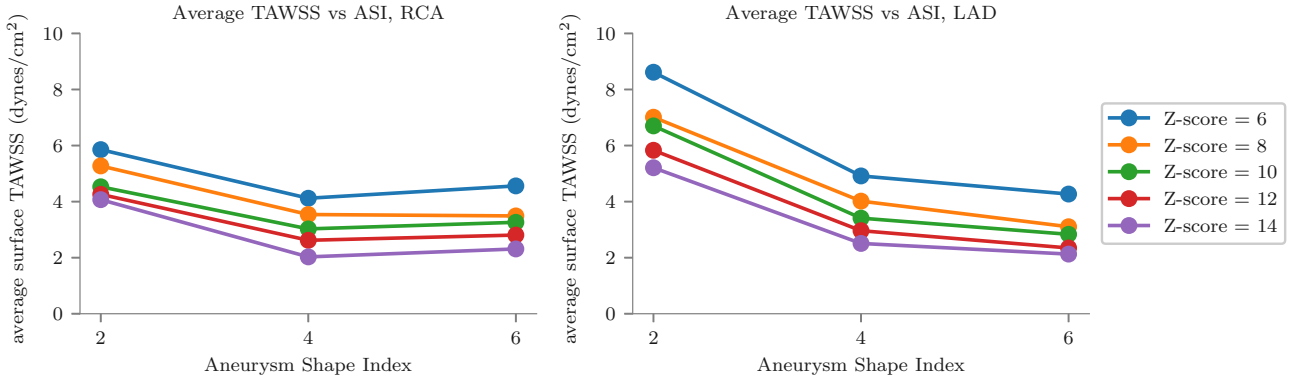


Figure 3: Plots of average TAWSS as a function of aneurysm shape index, stratified by aneurysm Z-score, in the RCA and LAD. Note differences between the RCA and LAD in the extent of average TAWSS decrease as aneurysms elongate.

To understand hemodynamic variations with geometric parameters, distributions of hemodynamic parameters are quantified in an aggregate manner, revealing that multiple combinations of aneurysm shape and diameter can produce similar hemodynamics. First, the average TAWSS over each aneurysm surface is computed and plotted with respect to ASI, stratified by aneurysm Z-score (**Figure 3**). As shape index increases (i.e. more elongated aneurysms), and as Z-score increases, average TAWSS declines. While in the LAD, the lowest values appear in the longest aneurysms of largest diameter, with relatively steep negative trend overall, average values in the RCA remain relatively similar; the lowest values are observed in aneurysms with ASI = 4.

The fractional aneurysm surface area exposed to TAWSS values less than a critical threshold S_{min} is another aggregate measure that has been proposed for evaluating CAA hemodynamics and stratifying patient risk [10-13]. A plot of fractional area exposed to low TAWSS as a function of ASI, again stratified by aneurysm Z-score is given in **Figure 4**. We observe that for aneurysms in both the RCA and LAD, the fractional area under 1 dyne/cm² increases as either of Z-score or ASI increase. Notably, the longest aneurysms of moderate Z-score (ASI = 6, Z-score = 8) produce similar values to shorter aneurysms of largest Z-score (ASI = 2, Z-score = 14). As with average TAWSS, multiple combinations of aneurysm shape and diameter can produce similar hemodynamics.

Residence Time (RT1), the time a parcel of fluid spends within an aneurysm, can also be used to understand CAA hemodynamics. We observe that RT1 varies consistently with respect to aneurysm shape and diameter (**Figure 5**). Increased RT1 relative to the baseline, computed in the original vessel without artificial aneurysms, indicates that all aneurysms regardless of shape and diameter exhibit fluid accumulation, likely due to recirculation and stagnation. While the small aneurysm diameter (Z-score =

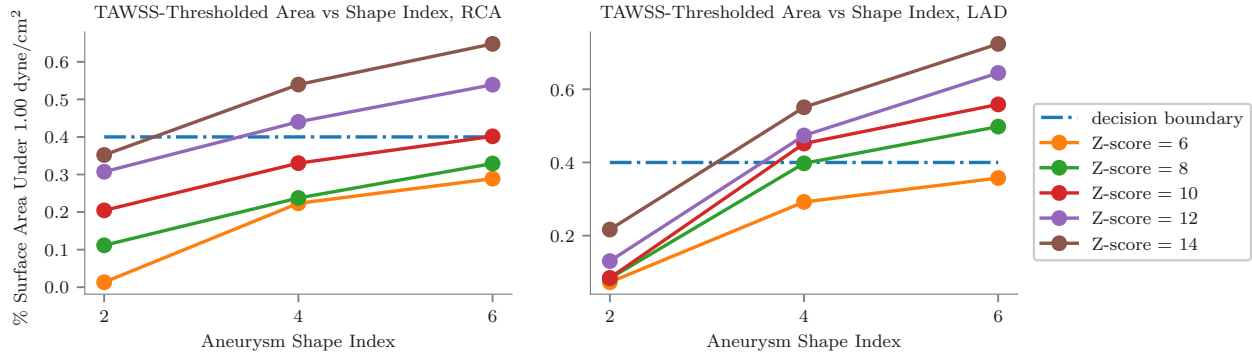


Figure 4: The percentage of wall surface area exposed to less than 1 dyne/cm², displayed with a decision boundary as would be used for clinical risk stratification. TAWSS-thresholded Area under this threshold exhibits increase with both ASI and Z-score increases.

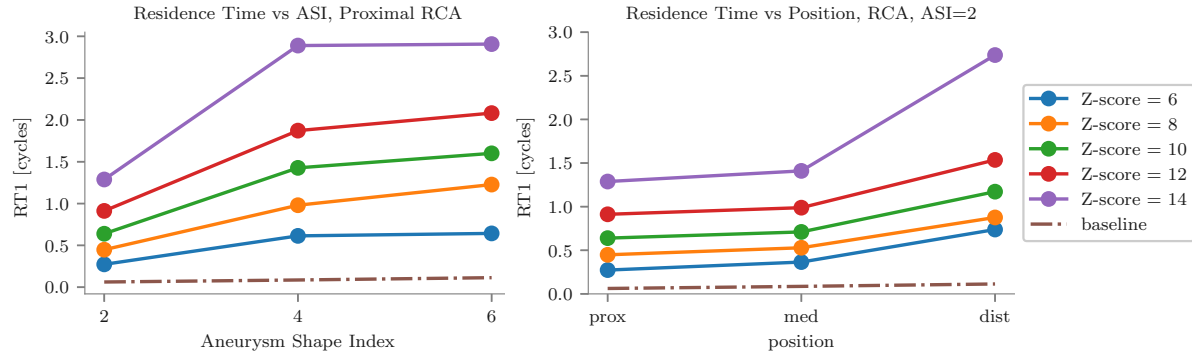


Figure 5: Plots of RT1 with respect to ASI and position, respectively; both plots show data stratified by aneurysm Z-score. As aneurysms elongate, increase in diameter, and move distally, RT1 increases.

6) produces little variation in RT1 as the aneurysm lengthens, higher values of Z-score tend to also magnify the effects of increasing aneurysm length. As with average TAWSS and fractional TAWSS-exposed area, the relationship between RT1 and aneurysm geometry indicates that multiple combinations of aneurysm shape and diameter can illicit similar hemodynamic behavior.

4.2 Aneurysm Position and Hemodynamics

Aneurysms generated in proximal, medial, and distal positions along the RCA enable comparison of hemodynamics as a function of position. Computing time-dependent flow rate into each aneurysm indicates that for each position, flow into the aneurysm is independent of diameter, but decreases with position along the centerline (**Figure 8**) due to the presence of additional branches diverting blood flow. Despite variation in flow rate, **Figure 7** depicts similar levels of TAWSS in aneurysms of the same shape

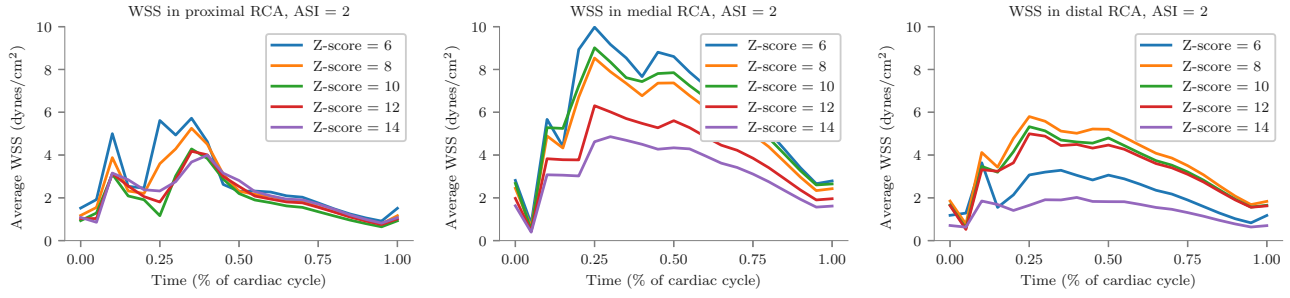


Figure 6: Plots of average WSS over time, at different positions along the RCA, for aneurysms with ASI = 2.

Proximal and medial positions show intuitive ranking in WSS value, but the distal RCA shows sharp significant decrease in average WSS for aneurysm of Z-score = 6 early in the cardiac cycle.

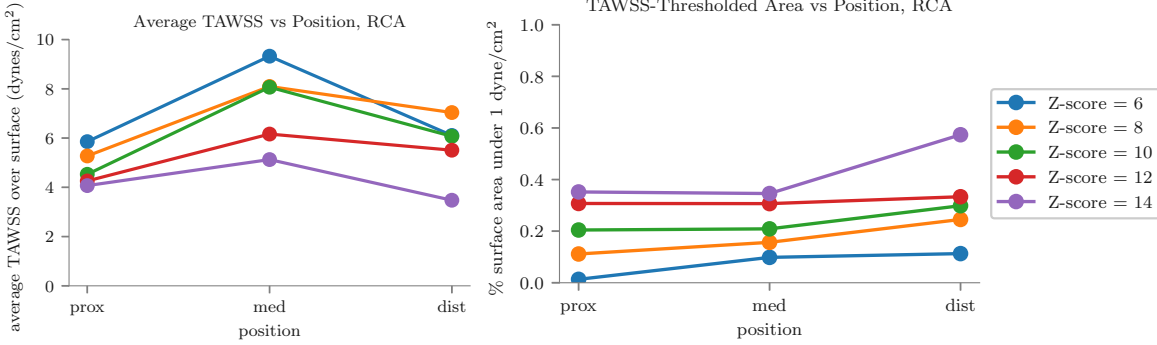


Figure 7: Plots of average TAWSS vs Position and TAWSS-Thresholded Area vs Position for aneurysms with ASI = 2 in the RCA. Although larger variation is seen in average TAWSS between proximal and medial positions, larger variation in TAWSS-Thresholded Area is seen as aneurysms move towards the distal position.

(ASI = 2). Proximal RCA aneurysms exhibit comparatively little variation in average TAWSS as Z-score increases, relative to medial and distal locations. Average TAWSS increases in medial aneurysms relative to proximal and distal positions, though fractional surface area exposed to low TAWSS exhibits little variation with respect to aneurysm geometry.

While average TAWSS and fractional TAWSS-exposed area exhibited inconsistent variation with respect to aneurysm position, RT1 increases consistently with respect to position (**Figure 5**). In particular, the largest, most distal aneurysm (Z-score = 14) has significantly increased RT1 relative to all other aneurysms of the same shape. **Figure 8** indicates that flow rates are identical for aneurysms in the same position regardless of diameter; especially given low variation in baseline RT1 with position, inlet flow rate differences fail to explain increased RT1 distally, as well as changes in RT1 with increased aneurysm diameter. This suggests that increased aneurysm diameter promotes pronounced recirculation in

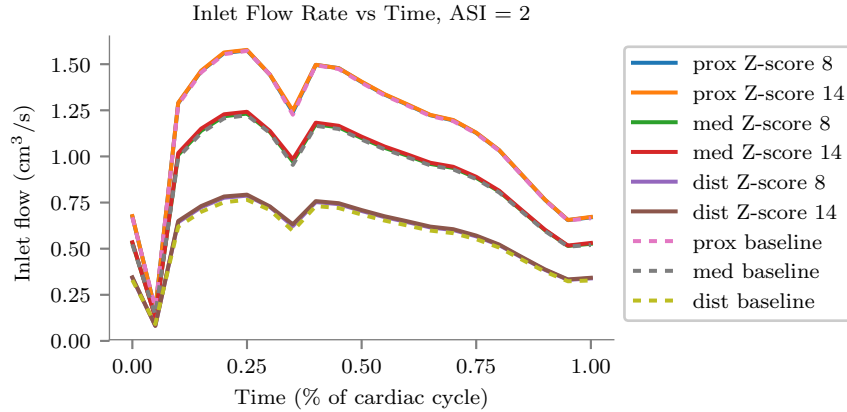


Figure 8: integrated velocities over a vessel cross section at the inlet of proximal, medial, and distal aneurysms demonstrates that inlet flow rates are not affected by aneurysm size (matching baseline values, shown as dashed lines). Rather, position influences flow rates due to the diversion of flow as a result of branching vessels. The coronary flow is out of phase with respect to aortic flow, as expected. The phase shift is relatively constant for all positions.

distal aneurysms relative to proximal or medial positions, enabling greater variation in RT1 with respect to aneurysm diameter.

To further investigate hemodynamic mechanisms underlying the non-linear relationship between average TAWSS and aneurysm position, we investigated average WSS over the cardiac cycle. We observe that in proximal and medial aneurysms of ASI=2 in the RCA, values of average WSS are ranked in decreasing order by Z-score over the cardiac cycle (**Figure 6**). However, in aneurysms in the distal RCA, intermediate values of Z-score (8, 10, 12) correspond to consistently increased values of average WSS compared to both low and high values (Z-score = 6, 14) throughout much of the cardiac cycle. This behavior can be understood through visualization of fluid velocity within the aneurysm.

Velocity streamlines through aneurysm cross sections reveal that inflow jet through the aneurysm expansion produces different impingement behaviors against the vessel wall (**Figure 9**). Aneurysms of the same position feature similar inflow jet patterns, producing the similar surface distributions of TAWSS as seen in **Figure 2**. In proximal and medial cases, increases in Z-score did not significantly alter inflow jet impingement area; however, in the distal cases, increases in Z-score alter the angle of the inflow jet, resulting in differing patterns of recirculation. These changes correspond to the WSS trends observed in **Figures 3, 6, 7** and the RT1 trends observed in **Figure 5**. Further, these inflow jet patterns explain how average TAWSS can increase in medial aneurysms without altering the fractional surface area exposed to low TAWSS (**Figure 7**).

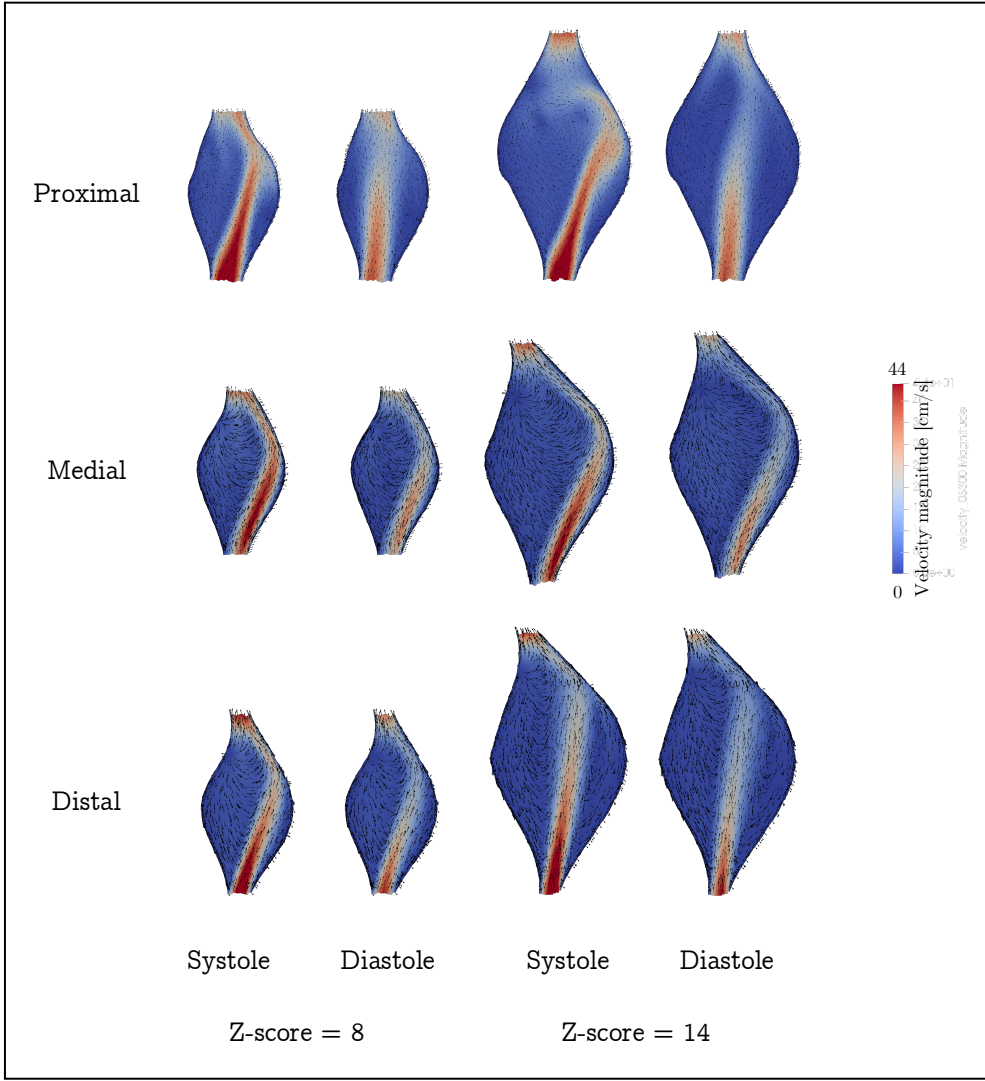


Figure 9: Aneurysm cross sections with velocity profiles displayed for two diameters of aneurysms at three different positions, at two points during the cardiac cycle. All systolic velocity profiles except for distal aneurysm, Z-score = 14 feature inlet jet impingement against the wall over a larger surface area. All aneurysms exhibit well-defined inlet jets.

Examining average TAWSS, fractional TAWSS-exposed area, and RT1 indicates that aneurysm diameter, shape, and position jointly determine aneurysm hemodynamics. Further, we find that aneurysm position influences hemodynamics by influencing inflow jet patterns, suggesting that local vessel curvature may be an effective low-dimensional predictor of hemodynamic behavior.

5 Discussion

The importance of accurate risk stratification methods for patients with CAAs secondary to KD is well understood. Indeed, studies over the last several years have shown the AHA's diameter-based algorithm for initiation of systemic anticoagulation to be insufficient for effectively predicting patient risk. Although these studies have explored the potential for patient-specific simulations to reveal key hemodynamic predictors underlying thrombotic risk, the variability of these predictors with respect to patient anatomy and aneurysm geometry has remained unclear.

An extensive pre- and post-processing pipeline was developed from scratch for systematic generation of idealized aneurysms and analysis of simulation results. Our idealized aneurysm models indicate that Z-score remains a strong predictor of hemodynamic behavior. Within **Figures 3-9**, we can still see the role of diameter – there are consistent trends in average TAWSS and RT1 with respect to Z-score at each level of ASI. However, Z-score alone is insufficient to determine hemodynamic behavior – shape and position, also, are influential (**Figures 3-5, 9**). Further, we highlight the potential for vessel curvature as an additional geometric parameter influencing hemodynamics (**Figure 9**).

Fraction of aneurysm surface area exposed to low TAWSS has been used to construct a decision boundary for KD patient risk classification that is more predictive of thrombosis than aneurysm diameter [10, 11]. Thus, we assess the distribution of TAWSS over the surface as one potential surrogate for hemodynamic behaviors that may underlie thrombosis. Results exemplified by **Figure 4** show aneurysms with constant diameter but with different aspect ratios, or with constant aspect ratio and varying diameter, can furnish substantially different hemodynamic environments. These consistent variations suggest that a combination of shape parameters may be sufficiently predictive of aneurysm hemodynamics, potentially reducing need for computationally expensive 3D simulations.

Additionally, varying both shape and diameter can give rise to similar hemodynamic parameters. This suggests that the effectiveness of TAWSS-thresholded area for patient risk stratification lies in its ability to capture critical hemodynamic features that are not strictly dependent on aneurysm shape or diameter alone. In comparison, averaging TAWSS over the surface of the aneurysm also affords a single-dimensional summary of aneurysm hemodynamics, but struggles to capture both variations in time and sacrifices knowledge of spatial distribution (**Figures 3, 6, 9**). With this in mind, it appears that utilization of average TAWSS for clinical risk stratification must be contextualized by the hemodynamic features lost during temporal and spatial averaging.

We also investigated changes in RT1 as aneurysm shape, diameter, and position vary. We find that RT1 increases consistently as Z-score, shape index increase, and as position becomes more distal. A

relationship between residence time and thrombosis has been hypothesized for both cerebral and coronary aneurysms [13, 17, 18]. Here, however, RT1 increases intuitively with both aneurysm length and diameter. Given relatively well-developed inlet jets as illustrated in **Figure 9** that may be unrealistic in true patient anatomies, it is difficult to determine whether these trends are a characteristic of the RT1 parameter, or whether geometric similarity between all smooth, symmetric idealized aneurysms in this study inhibits analysis of RT1's ability to quantify nuanced hemodynamics.

Although we have systematically investigated the role of shape parameters on aggregate measures of aneurysm hemodynamics, further work should continue to investigate the potential for low-dimensional representations of aneurysm geometry towards predicting CAA hemodynamics as a surrogate for improving clinical predictive value. Known correlations between aneurysm hemodynamic and geometric features suggest potential to link clinical measurements easily obtained from echocardiography or other routine imaging modalities with patient outcome. Such approaches may form the basis for more sophisticated geometry-based risk stratification methods supporting clinical decision-making in assessment of KD patients.

We demonstrate the potential for modification of patient-specific vascular models and artificial aneurysm generation for systematic evaluation of the relationship between anatomy and hemodynamics. Extending the methodology in [10, 11], we first illustrate that controlled variation in aneurysm shape, diameter, and position may produce predictable variation in hemodynamic parameters. Indeed, assumptions such as axisymmetric aneurysm radius, high degree of surface smoothness, and single aneurysm per vessel limit clinical realism. Even with these simplifying assumptions, we demonstrate that manipulating key geometric parameters such as length, diameter, and position are sufficient to enable systematic variation of aneurysm hemodynamics, allowing closer interrogation of inconsistent variations in hemodynamics. Overall, the use of vessel modification pipeline for systematic understanding of CAA hemodynamics in KD patients forms the foundation for future systematic hemodynamic studies that may inspire insight into disease pathogenesis, aid validation of patient-specific risk stratification methods, and help characterize cardiovascular surgical interventions.

6 Acknowledgements

I am deeply thankful for Dr. Alison Marsden. Since I first joined the group as a sophomore, her tremendous support and guidance have allowed me to grow in ways I could not have imagined and cement my passion in this fascinating interdisciplinary space.

Additionally, I would like to thank Dr. Marsden and Dr. James Priest for reading this thesis; without their time and dedication, this would not have been possible.

I am incredibly thankful for my mentor, Marsden lab graduate student Noelia Grande Gutiérrez for her mentorship, and for fielding my long streams of questions over the last few years. Her mentorship has pushed me to constantly improve, and has allowed me to develop this independent work.

I am also thankful for the other members of the Marsden lab who have made the last few years so wonderful and enriching.

Perhaps most importantly, I'd like to thank my friends and my parents for their unconditional support and encouragement. Thank you all for weekly phone calls, regular memes, and the endless warmth that have been with me through every twist and turn, and for making me who I am. I never know how to thank you all enough.

7 References

- [1] Burns JC, Shike H, Gordon JB, Malhotra A, Schoenweiter M, Kawasaki T. Sequelae of Kawasaki disease in adolescents and young adults. *J Am Coll Cardiol.* 1996;28(1):253-257. Doi:10.1016/0735-1097(96)00099-X
- [2] Burns JC. Kawasaki Disease update. *Indian J Pediatr.* 2009;76(1):71-76.
Doi:<http://dx.doi.org/10.1007/s12098-009-003103>.
- [3] Kato H, Sugimura T, Akagi T, Sato N, Hashino K, Maeno Y, Kazue T, Eto G, Yamakawa R. Long-term consequences of Kawasaki disease A 10- to 21-year follow up study of 594 patients. *Circulation.* 1996;94:1379-1385.
- [4] Rizk SRY, El Said G, Daniels LB, et al. Acute myocardial ischemia in adults secondary to missed Kawasaki disease in childhood. *Am J Cardiol.* 2015;115(4):423-427. Doi:10.1016/j.amjcard.2014.11.024
- [5] McCrindle BW, Rowley AH, Newburger JW, Burns JC, Bolger AF, Gewitz M, Baker AL, Jackson MA, Takahashi M, Shah PB, Kobayashi T, Wu MH, Saji TT, Pahl E, American Heart Association Rheumatic Fever Ed, and Kawasaki Disease Committee of the Council on Cardiovascular Disease in the Young, Nursing CoCaS, Anesthesia CoCSa, Prevention aCoEa. Diagnosis, treatment, and long-term management of Kawasaki disease: A scientific statement for health professionals from the American Heart Association. *Circulation.* 2017; 135:e927-e999.
- [6] Tsuda E, Hirata T, Matsuo O, Abe T, Sugiyama H, Yamada O. The 30-year outcome of patients after myocardial infarction due to coronary artery lesions caused by Kawasaki disease. *Pediatr Cardiol.* 2011;32(2):176-182. doi:10.1007/s00246-010-9838-y.
- [7] Grande Gutierrez N, Shirinsky O, Gagarina N, Lyskina G, Fukazawa R, Ogawa S, Burns JC, Marsden AL, Kahn AM. Assessment of coronary artery aneurysms caused by Kawasaki disease using transluminal attenuation gradient analysis of computerized tomography angiograms. *Am J Cardiol.* 2017;120:556-562.
- [8] Senzaki H. Long-term outcome of Kawasaki disease. *Circulation.* 2008;118(25):2763-2772.
Doi:10.1161/CIRCULATIONAHA.107.749515.
- [9] Ohkubo T, Fukazawa R, Ikegami E, Ogawa S. Reduced shear stress and disturbed flow may lead to coronary aneurysm and thrombus formation. *Pediatr Int.* 2007;49:1-7.
- [10] Grande Gutierrez N, Matthew M, McCrindle BW, et al. Hemodynamic variables in aneurysms are associated with thrombotic risk in children with Kawasaki disease. *International Journal of Cardiology.* 2019;281:15-21. Doi:10.1016/J.IJCARD.2019.01.092.
- [11] Grande Gutierrez N, Kahn A, Burns JC, Marsden AL. Computational blood flow simulations in Kawasaki disease patients: Insight into coronary artery aneurysm hemodynamics. *Global Cardiology Science & Practice.* 2017;29
- [12] Sengupta D, Kahn AM, Burns JC, Sankaran S, Shadden SC, Marsden AL. Image-based modeling of hemodynamics in coronary artery aneurysms caused by Kawasaki disease. *Biomech Model Mechanobiol.* 2012;11:915-932.

- [13] Sengupta D, Kahn AM, Kung E, Esmaily Moghadam M, Shirinsky O, Lyskina GA, Burns JC, Marsden AL. Thrombotic risk stratification using computational modeling in patients with coronary artery aneurysms following Kawasaki disease. *Biomech Model Mechanobiol.* 2014;13:1261-1276.
- [14] Updegrove A, Wilson NM, Merkow J, Lan H, Marsden AL, Shadden SC. Simvascular: An open source pipeline for cardiovascular simulation. *Ann Biomed Eng.* 2017; 45:525-541.
- [15] Dallaire F, Dahdah N. New equations and a critical appraisal of coronary artery Z scores in healthy children. *J Am Soc Echocardiography.* 2011;24(1):60-74. doi:10.1016/j.echo.2010.10.004
- [16] H. Si. TetGen, a Delaunay-Based Quality Tetrahedral Mesh Generator. *ACM Trans. On Math. Software.* 2015;41(11).
- [17] Esmaily Moghadam M, Hsia T-Y, Marsden AL. A non-discrete method for computation of residence time in fluid mechanics simulations. *Phys Fluids (1994).* 2013;25(11);110802. doi:10.1063/1.4819142
- [18] Ngoepe MN, Frangi AF, Byrme JV, Ventikos Y. Thrombosis in Cerebral Aneurysms and the Computational Modeling Thereof: A Review. *Front Physiol.* 2018;9:306. Published 2018 Apr 4. doi:10.3389/fphys.2018.00306